



Design of a renewable hydroxyapatite-biocarbon composite for the removal of uranium(VI) with high-efficiency adsorption performance

Jun Liao¹ · Ting Xiong¹ · Ling Ding¹ · Ying Xie¹ · Yong Zhang¹ · Wenkun Zhu¹

Received: 19 February 2022 / Accepted: 8 May 2022
© The Author(s) 2022

Abstract

The hydroxyapatite-loaded swine manure derived-biocarbon was successfully prepared by pyrolysis method for the adsorption of uranium(VI). The results of the adsorption experiments displayed that the adsorption behaviors for uranium(VI) of biocarbon did almost not depend on the interfering ions except Al^{3+} , Ca^{2+} and CO_3^{2-} , showing the high selectivity of the composites for uranium(VI). The maximum static and dynamic removal capacity of the hydroxyapatite-biocarbon composites to uranium(VI) were 834.8 and 782.8 mg/g (pH = 3, m/V = 0.1 g/L and T = 298 K), far exceeding other reported biocarbon and hydroxyapatite materials, which indicated that the hydroxyapatite-biocarbon composites possessed an application potential in adsorption. After five cycles of adsorption–desorption processes, the removal efficiency of the hydroxyapatite-biocarbon composite for uranium(VI) was 93.2% ($C_i = 5$ mg/L, pH = 3, m/V = 0.1 g/L and T = 298 K), revealing that the composite had excellent stability and reusability. Moreover, the capture mechanisms of the hydroxyapatite-biocarbon composite for uranium(VI) included ion exchange and complexation, which was ascribed to the ample active adsorption sites ($-\text{OH}$ and PO_4^{3-}). Therefore, the hydroxyapatite-loaded swine manure derived-biocarbon would be a potential material to effectually separate uranium(VI) from solution.

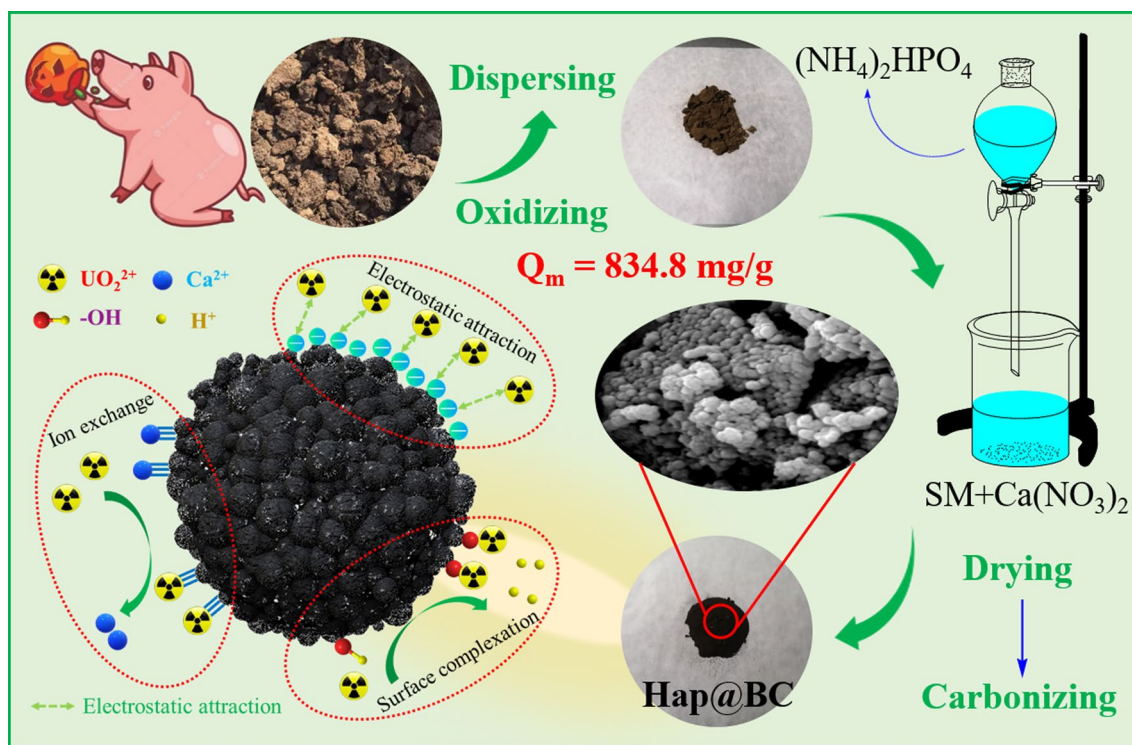
Jun Liao and Ting Xiong contributed equally to this study

✉ Yong Zhang
pandmzy@foxmail.com

✉ Wenkun Zhu
zhuwenkun@swust.edu.cn

¹ State Key Laboratory of Environment-Friendly Energy Materials, Sichuan Co-Innovation Center for New Energetic Materials, National Co-Innovation Center for Nuclear Waste Disposal and Environmental Safety, Nuclear Waste and Environmental Safety Key Laboratory of Defense, School of National Defence Science & Technology, Southwest University of Science and Technology, Mianyang 621010, China

Graphical abstract



Highlights

1. The recyclable high-efficiency Hap@BC was prepared for U(VI) removal.
2. The adsorption capacity for U(VI) of Hap@BC-10% achieved 834.8 mg/g.
3. The U(VI) extraction efficiency reached 99.9% in dynamic adsorption.
4. The interaction mechanism between U(VI) and Hap@BC was clearly expounded.

Keywords Hap@BC · Adsorption · Uranium(VI) · Regeneration · Interaction mechanism

1 Introduction

Uranium(VI) (U(VI)) is the most widely distributed natural radioactive metal element in the earth's crust, which can be applied in nuclear energy engineering fields due to its efficient and economic characteristics (El-Maghrabi et al. 2019). With the rapid development of the global nuclear industry, a large amount of U(VI)-containing wastewater has been produced from several industrial activities, such

as fossil fuel extraction and development of nuclear weapons, resulting in the increase of potential risks and threats to natural environment and human health (Lei et al. 2022; Tal et al. 2022). For example, the excessive exposure of U(VI)-containing wastewater will lead to serious diseases to creatures such as nephritis, neurological disorders and even cancer (Jin et al. 2021). Therefore, the removal of U(VI) from wastewater before discharge became a hot topic in many research areas. In recent years, a series of solid materials have been developed to remove U(VI) from wastewater, such as hydroxyapatite (Hap), biocarbon, metal oxides and resin (Liao et al. 2021; Yue et al. 2021; Hu et al. 2020).

Among these materials, Hap, a typical Ca-P mineral, which generally exists in hard tissues and phosphate mineral rocks, possesses a high removal capacity and efficiency for the numerous divalent cations owing to its high stability and unique crystal structure (Hassanein et al. 2021). However, the pure nano-Hap (nHap) is easy to agglomerate during use, resulting in many active sites on nHap to be coated and hidden, which will greatly inhibit its ability to remove pollutants (Zhou et al. 2021; Biedrzycka et al. 2021). Therefore, it is important to avoid the agglomeration behavior of Hap for improving its adsorption performance. It is reported that

Hap can be evenly loaded on suitable support materials, such as graphene, carbon nanotubes, MXene and polymer materials, which will effectively prevent its agglomeration behavior and improve its adsorption performance. For example, Su et al. (2021) prepared a graphene oxide material functionalized with nHap to efficiently remove uranium(VI) (U(VI)) in solution with excellent adsorption performance and the maximum removal capacity of the composite material was 373 mg/g. Wang et al. (2017) obtained a Hap-loaded carbon nanotube material through hydrothermal method, which showed a strong response to heavy metal ions. Kede et al. (2012) reported a polymer material loaded with Hap, which showed that the in-situ adsorption performance of Hap to metal ions could be greatly improved by dispersing Hap on polymer. However, the application of these support materials in treating wastewater was limited owing to the high cost of graphene and carbon nanotubes and the complex synthesis process of polymers (Qin et al. 2021; Son and Park 2019; Choong et al. 2021). Therefore, it was very important to develop a support material with low cost and simple preparation process to prevent the agglomeration behavior of Hap.

In recent years, Hap is usually loaded on other economical materials to reduce cost, such as biocarbon (BC), g-C₃N₄ and metal oxide. Among these materials, BC is widely applied as a support material of Hap in the remediation of water environment due to its excellent physical properties (high specific surface area and good dispersion) and plenty active functional groups related to the affinity of heavy metals (Zhou et al. 2022; Chen et al. 2021a). Besides, BC was an environment-friendly material that were usually prepared by thermochemical conversion of animal and plant residues, which not only realized the reuse of waste, but also reduced the carbon emissions (Dong et al. 2021; Huang et al. 2019; Liang et al. 2021). Especially, the animal manure-derived BC has attracted extensive attention in removing heavy metals (Idrees et al. 2018; Qiu et al. 2021). Considering the advantages of Hap and animal manure-derived BC, the combination of these two materials might obtain a novel and efficient material for the remediation of wastewater. In depth, loading Hap on the surface of BC could provide abundant functional groups for BC and Hap possessed great affinity to divalent cation, which would increase the adsorption potential of BC (Ahmed et al. 2021). However, the adsorption performance of the composite would be limited due to the agglomeration of excessive Hap particles and the loss of active sites in pyrolysis process (Li et al. 2019). Therefore, it is significance to explore the effects of the doping amount of Hap on the adsorption performance of BC. Moreover, Hap-based materials were extremely difficult to reuse, indicating that the development of a renewable Hap-based material is meaningful.

In this work, three kinds of Hap-BC composites with different content of Hap were prepared using swine manure

(SM) as the biocarbon source and the adsorption properties of the composites were evaluated with U(VI) as cation source. The purpose of this paper was: (1) to provide a new idea for reasonable treatment of the SM, (2) to prepare a renewable Hap-loaded biocarbon for U(VI) adsorption, (3) to discuss the effect of the content of Hap on U(VI) adsorption behavior, and (4) to research in depth the capture mechanisms of the Hap-BC composite for U(VI).

2 Experimental

2.1 Reagents and chemicals

SM was obtained from a piggery in Sichuan Province, which was directly used after strong dispersion. Hydrochloric acid (36.0–38.0%), NaOH (98.0%), Ca(NO₃)₂ (> 97.5%), (NH₄)₂HPO₄ (98.5%), Na₂CO₃ (99.8%), NaNO₃ (99.5%), NaClO₄·H₂O (99.5%), Na₂SO₄ (99.5%), Na₃PO₄ (99.5%), NaCl (99.5%), KCl (99.5%), CaCl₂ (96.0%), MgCl₂ (99.0%), AlCl₃·6H₂O (97.0%) and ZnCl₂ (98.0%) were obtained from Chengdu Chron Chemicals. Arsenazo (III) (99.9%) and UO₂(NO₃)₃·6H₂O (> 99.5%) were purchased from Aladdin Industrial Corporation. Deionized water was used throughout the experiment.

2.2 Preparation of Hap-BC composite

2.2.1 Preparation of modified SM

The collected SM was dispersed with strong stirring in deionized water for 1 h to remove the soluble organic substance. After drying, the solid was immersed in KMnO₄ solution with a concentration of 0.1 mol/L for the surface modification of SM. Then, the modified SM was dried under natural pressure at 60 °C for 24 h.

2.2.2 Preparation of Hap@BC-5%, Hap@BC-10% and Hap@BC-15%

About 9 g of the modified SM was strongly dispersed in 50 mL of Ca(NO₃)₂ solution (0.2 mol/L) to obtain a suspension. Subsequently, 50 mL of (NH₄)₂HPO₄ solution (0.12 mol/L) was slowly dripped into the suspension under vigorously stirring to prepare the SM-Hap suspension, which was freeze-dried for about 50 h to gain the SM-Hap composite. Then, the SM-Hap composite was pyrolyzed at 500 °C under nitrogen atmosphere for 2 h to synthesize Hap-BC composite (The mass percentage of Hap was 10%), which was named Hap@BC-10%. Finally, Hap@BC-5% and Hap@BC-15% were prepared according to the same method. Moreover, the modified SM was directly calcined to prepare pure bio-carbon (BC).

2.3 Characterization and batch experiments

FT-IR spectra were recorded on a fourier transform infrared spectroscope (FT-IR, 380FT-IR, America) in the range between 4000 and 400 cm^{-1} . The crystallographic structures were determined via a powder X-ray diffractometer (XRD, TD3500, China) with Cu-K α radiation over the 2 θ range from 3 to 80° (10°/min). The specific surface area and pore size distribution were characterized by N₂ adsorption–desorption analyser (ASAP 2460 3.01, America) and the corresponding data analysis was estimated by using Brunauer–Emmett–Teller (BET) and Barrett–Joyner–Halenda (BJH) methods, respectively. The morphology of BC, Hap@BC-5%, Hap@BC-10% and Hap@BC-15% was characterized by scanning electron microscopy (SEM, Ultra55, Germany).

In this work, a certain amount of UO₂(NO₃)₃·6H₂O was dissolved in 100 mL of nitric acid (0.1 mol/L) and then diluted to 1 L with deionized water to obtain uranyl solution. The adsorption properties of Hap@BC-5%, Hap@BC-10% and Hap@BC-15% towards U(VI) were evaluated through batch experiments under different conditions, such as different initial pH, different initial U(VI) concentration, different interfering ions, different ionic strength and different contact time. Before adsorption, hydrochloric acid solution (pH=1) and NaOH solution (pH=13) were used to adjust the initial pH of U(VI) solution. After adsorption, the polyethersulfone filter (0.22 μm) was used to separate Hap@BC from solution. The U(VI) concentration in solution was assessed using a UV–vis spectrophotometry at the wavelength of 651 nm (UV, UV-1900PC) (Chen et al. 2021b; Wang et al. 2021). The equilibrium removal percentage (RP, %) and adsorption capacity (Q_e , mg/g) of Hap@BC for U(VI) could be calculated according to the adsorbent mass (m , mg), liquid volume (V , mL), equilibrium concentration of U(VI) (C_e , mg/L) and initial concentration of U(VI) (C_i , mg/L) (Eqs. 1 and 2). Moreover, the structure of Hap@BC-10% and Hap@BC-10%-U was analyzed using X-ray photoelectron spectroscopy (XPS, Thermo Scientific K-Alpha, America), scanning electron microscopy (SEM, Ultra55, Germany), Fourier-transform infrared spectrometer (FT-IR, 380FT-IR, America) and powder X-ray diffractometer (XRD, TD3500, China) to explore the removal mechanism of Hap@BC to U(VI).

$$Q_e = \frac{C_i V - C_e V}{m} \quad (1)$$

$$RP = \frac{C_i - C_e}{C_i} \times 100\% \quad (2)$$

3 Results and discussion

3.1 Characterization

As shown in Figure S1, the bulk SM was transformed into powder after KMnO₄ pretreatment. The Hap nanoparticles were in-situ formed on the surface of modified SM via precipitation method to obtain gray white solid (SM-Hap composite). Then, the SM-Hap composite was pyrolyzed at 500 °C under nitrogen atmosphere to gain the black Hap-BC composite. It was worth mentioning that the Hap-BC composite possessed fluffy structure, which could be conducive to the U(VI) adsorption in solution. Besides, the preparation of Hap-BC composite using SM as the raw material could not only solve the problem of soil damage caused by nutrient elements in SM, but also reduce the risk of water damage caused by U(VI)-containing wastewater.

The structure and morphology of Hap@BC-5%, Hap@BC-10% and Hap@BC-15% were analyzed by FT-IR spectra, XRD patterns, N₂ adsorption desorption curves and SEM images. As shown in Fig. 1a, the broad peak of BC at about 1053 cm^{-1} was attributed to the stretching vibration of C–O bonds. After the incorporation of Hap, two new peaks were observed at 1040 and 1072 cm^{-1} , which were the characteristic bands of the phosphate stretching vibrations, proving that Hap was successfully incorporated into BC (Xuan et al. 2022; Han et al. 2022; Wu et al. 2019). The XRD patterns of BC, Hap@BC-5%, Hap@BC-10% and Hap@BC-15% are shown in Fig. 1b. With the increase of Hap content, the crystallization peak of BC significantly weakened and the new diffraction peaks at 31.9, 32.4 and 33.0° were observed, which corresponded to (211), (300) and (202) plane of Hap, respectively (Londoño-Restrepo et al. 2020; Ferreira et al. 2022), indicating that Hap nanoparticles were doped into BC through chemical bonding due to the altered crystallinity of the BC-based material (Li et al. 2022).

As shown in Fig. 1c, the N₂ adsorption–desorption isotherms of Hap@BC-5%, Hap@BC-10% and Hap@BC-15% belonged to type IV with a distinct hysteresis loop ($P/P_0 > 0.4$), indicating that Hap@BC-5%, Hap@BC-10% and Hap@BC-15% had complex and disorder pore structure (Wu et al. 2019), which were further confirmed by the BJH pore size distributions (Fig. 1d). Besides, comparing Hap@BC-5% (128.6 m^2/g) with Hap@BC-10% (155.2 m^2/g), the increase in specific surface area might be attributed to the formation of some narrow and deep pores during the precipitation of Hap nanoparticles (El-Maghrabi et al. 2019). The specific surface area of Hap@BC-15% (125.4 m^2/g) decreased due to the aggregation of excessive Hap nanoparticles.

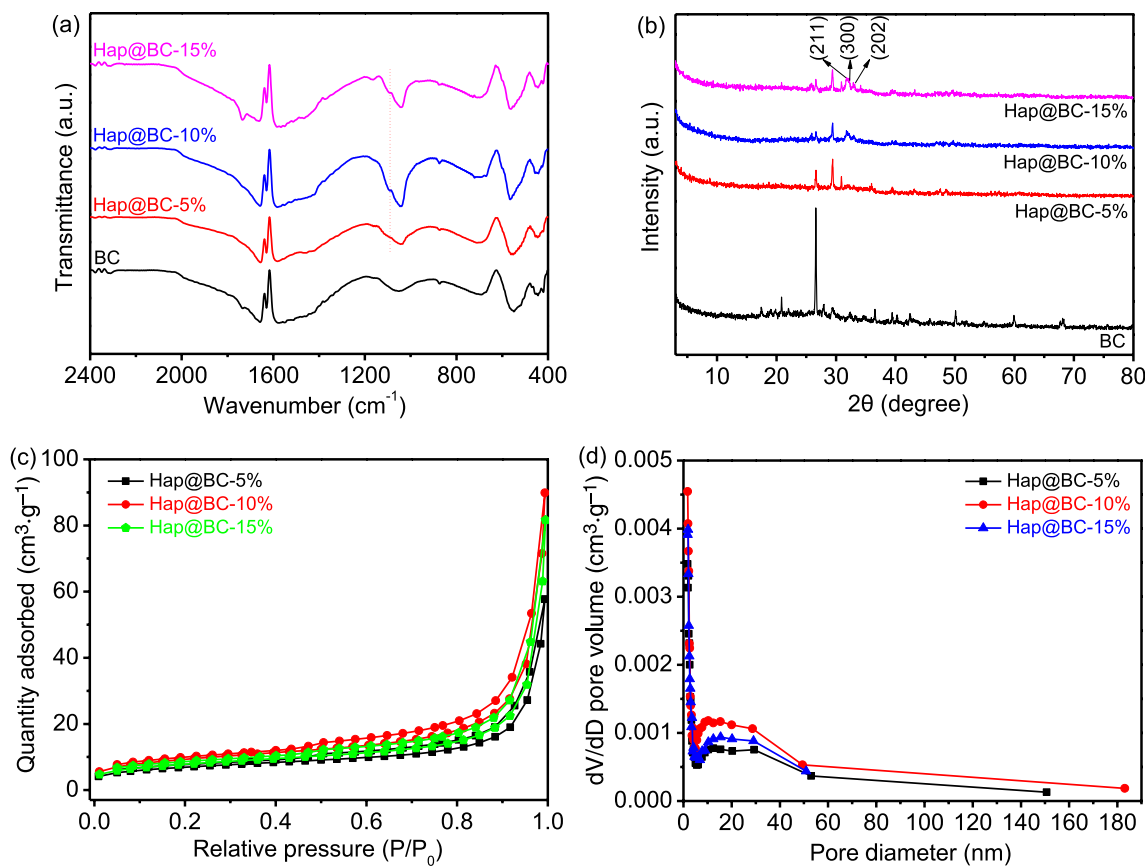


Fig. 1 a FTIR spectra, b XRD patterns of BC, Hap@BC-5%, Hap@BC-10% and Hap@BC-15%, c N₂ adsorption–desorption isotherms and d BJH pore size distributions of Hap@BC-5%, Hap@BC-10% and Hap@BC-15%

The SEM images were used to analyze the morphology of the obtained BC, Hap@BC-5%, Hap@BC-10% and Hap@BC-15% (Figure S2). It was observed that the surface of BC had microporous and fluffy structure, which could provide the suitable location for the adsorption of U(VI) on the surface. After doping Hap nanoparticles, many fine particles were adhered to the surface of BC, which could raise the contact points for U(VI) in the solution. However, as the content of Hap nanoparticles increased, the carbon layers with dense structure appeared in Hap@BC-15% and the heterogeneous agglomerates were randomly attached on the carbon layers, which might cause the coating of active sites, thereby reducing its U(VI) adsorption ability.

3.2 Adsorption

3.2.1 Effect of pH

The surface charge of adsorbent and the ionization degree of U(VI) might be changed with the change of pH value, which showed that the pH value of solution was an important factor in the removal process (Verma and Kim 2022; Nezhad et al. 2021). As shown in Fig. 2a, the removal percentage

of U(VI) first increased sharply and then decreased slowly with the pH of the solution increasing from 2 to 10. At the optimum pH (pH = 3), the maximum removal percentage of Hap@BC-5%, Hap@BC-10% and Hap@BC-15% reached 94.9%, 98.7% and 95.7%, respectively ($C_i = 5$ mg/L and $m/V = 0.1$ g/L). As expected, Fig. 2b shows that the change of the adsorption efficiency of Hap@BC-5%, Hap@BC-10% and Hap@BC-15% to U(VI) followed the similar trend at high concentrations ($C_i = 50$ mg/L). It was interesting to note that Hap@BC-10% still possessed a strong adsorption ability for U(VI) even at high U(VI) concentrations, which indicated that Hap@BC-10% has a potential to be applied to high-efficiency separation of U(VI) at large-scale level.

For further studying the removal behavior of Hap@BC-5%, Hap@BC-10% and Hap@BC-15% for U(VI) at various pH, the existing forms of U(VI) species at different pH were simulated and the surface charge of the adsorbent at different pH was studied. As displayed in Fig. 2c and d, U(VI) species in the solution with the pH in the range from 2 to 4 mainly existed in the form of free uranyl ions (UO_2^{2+}). When the pH increased from 4 to 7, U(VI) began to form uranyl/hydroxy complexes, such as $UO_2(OH)^+$, $UO_2(OH)_2$ (aq), $(UO_2)_4(OH)_7^+$ and $(UO_2)_3(OH)_5^+$ (Zhu et al. 2018).

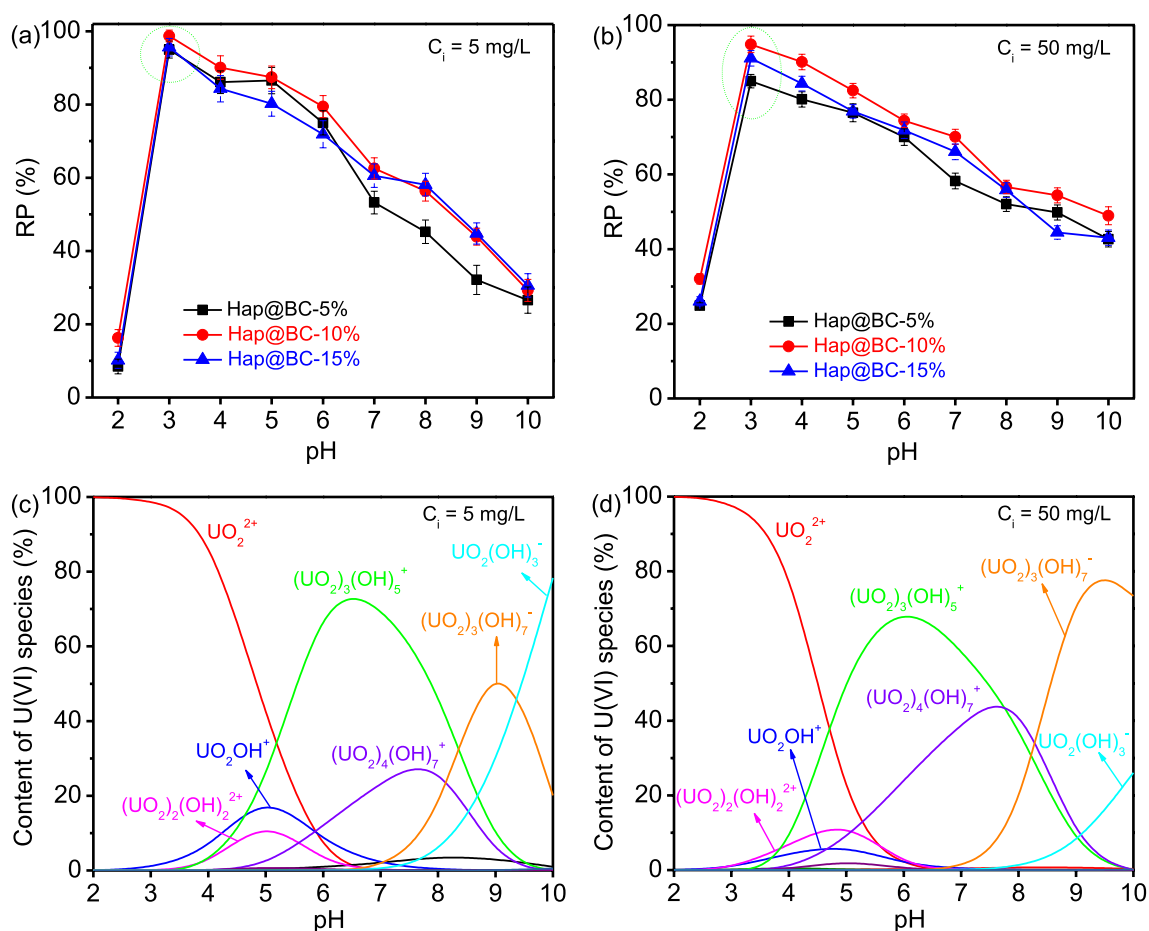


Fig. 2 **a** Effect of pH on U(VI) removal by Hap@BC-5%, Hap@BC-10% and Hap@BC-15% ($T=298$ K, $m/V=0.1$ g/L and $C_i=5$ mg/L), **b** Effect of pH on U(VI) removal by Hap@BC-5%, Hap@BC-10% and Hap@BC-15% ($T=298$ K, $m/V=0.1$ g/L and

$C_i=50$ mg/L), **c** Effect of pH on the existing forms of U(VI) species ($T=298$ K and $C_i=5$ mg/L) and **d** Effect of pH on the existing forms of U(VI) species ($T=298$ K and $C_i=50$ mg/L)

When pH exceeded 7, U(VI) species were further complexed with OH^- to form the negatively charged complexes due to the increasing concentration of OH^- in the solution (Li et al. 2018; Song et al. 2019). When UO_2^{2+} ions were transformed into uranium hydroxide complexes with stable structure, the adsorption affinity of the adsorbent to U(VI) species would decrease sharply due to the occupation of sites of U(VI) species (Liu et al. 2022; Zhu et al. 2021). Moreover, the pH value at the zero-charge point (pH_{zcp}) was estimated via potentiometric titration. As shown in Figure S3, the pH_{zcp} value of Hap@BC-10% was 6.23, which illustrated that the surface potential of the Hap@BC-10% showed a negative charge when $pH < 6.23$, while the particles showed a positive charge when $pH > 6.23$ (Wang et al. 2022). In other words, the binding sites on Hap@BC-10% tended to be protonated in combination with H^+ at low pH ($pH < 3$). As the pH increased to 3, the protonation degree of Hap@BC-10% decreased, which would lead to the enhancement of the chelation with UO_2^{2+} . Besides, an ionization of the Hap

nanoparticles loaded on Hap@BC-10% occurred at $pH = 3$, supplying the adsorption system with phosphate ions which have high affinity for U(VI), precipitating and forming a new phase of $H_2(UO_2)_2(PO_4)_2 \cdot 8H_2O$ (Guo et al. 2020a). With the continuous rising of pH ($3 < pH < 6$), although the surface of Hap@BC-10% was negatively charged, the response of Hap@BC-10% to U(VI) species was decreased because $-OH$ occupied the sites of U(VI) species. In general, Hap@BC-10% possessed excellent adsorption ability at $pH = 3$, which was mainly ascribed to the weakening of the protonation degree of the Hap@BC-10% and the enhancement of the adsorption affinity between Hap and UO_2^{2+} .

3.2.2 Effect of the type and strength of interfering ions

The high selectivity for U(VI) is a crucial standard to assess the application value of adsorbent owing to a large number of common interfering ions in radioactive wastewater (Zhang et al. 2019; Ahmad et al. 2021). As shown in Fig. 3a

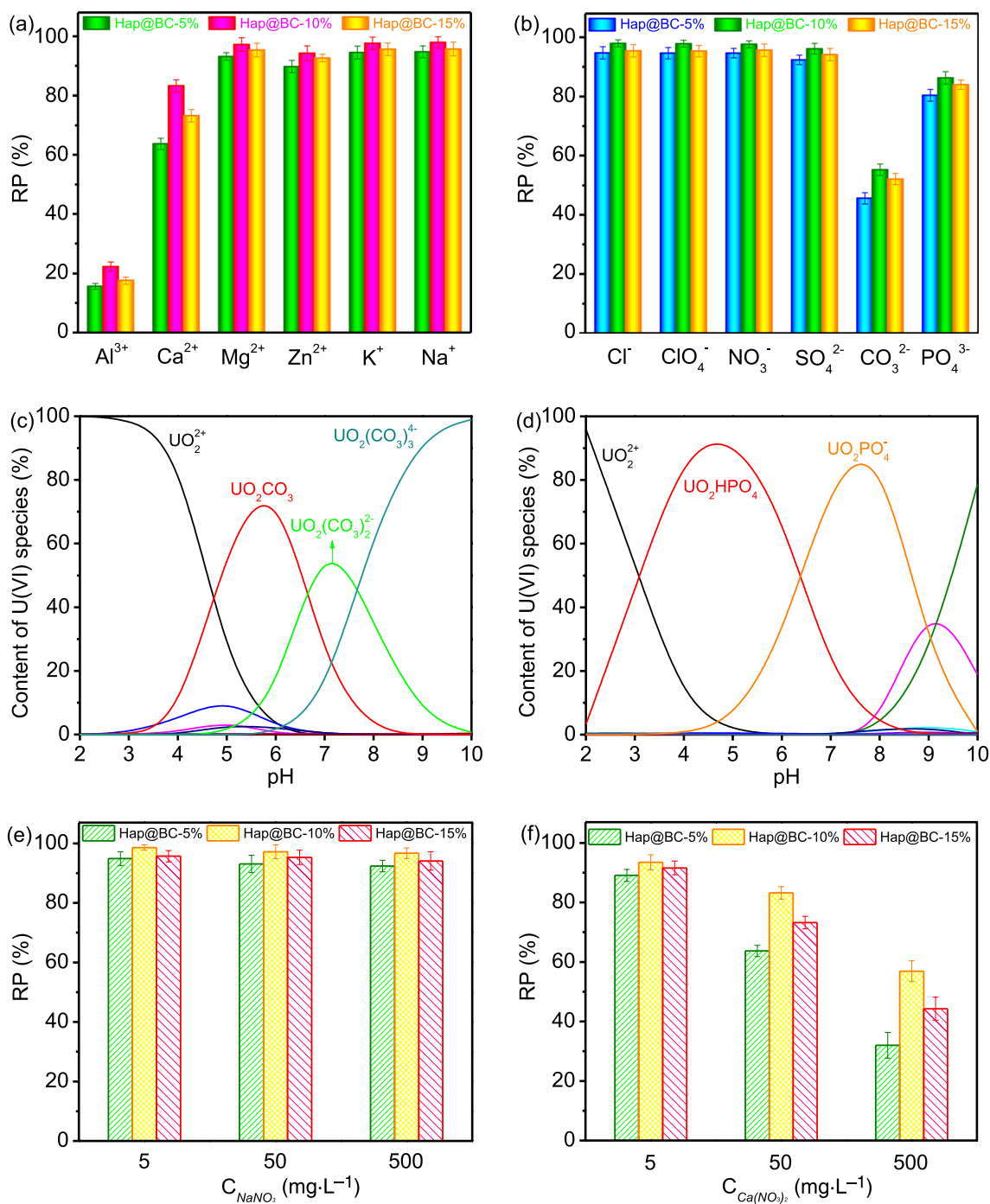


Fig. 3 a Effect of interfering cations on U(VI) removal by Hap@BC-5%, Hap@BC-10% and Hap@BC-15% (T=298 K, pH=3, m/V=0.1 g/L and C_i=5 mg/L), b Effect of co-existing anions on U(VI) removal by Hap@BC-5%, Hap@BC-10% and Hap@BC-15% (T=298 K, pH=3, m/V=0.1 g/L and C_i=5 mg/L), c Effect of CO₃²⁻ (50 mg/L) on the existing forms of U(VI) species (C_i=5 mg/L and T=298 K), d Effect of PO₄³⁻ (50 mg/L) on the existing forms

of U(VI) species (C_i=5 mg/L and T=298 K), e Effect of Na⁺ ions strength on U(VI) removal by Hap@BC-5%, Hap@BC-10% and Hap@BC-15% (T=298 K, pH=3, m/V=0.1 g/L and C_i=5 mg/L) and f Effect of Ca²⁺ ions strength on U(VI) removal by Hap@BC-5%, Hap@BC-10% and Hap@BC-15% (T=298 K, pH=3, m/V=0.1 g/L and C_i=5 mg/L)

and b, it was quite clear that the influence of interfering ions on the U(VI) removal of Hap@BC-5%, Hap@BC-10% and Hap@BC-15% was comparatively weak, suggesting that

the Hap@BC materials might possess a strong adsorption affinity and ability to U(VI) and it was a suitable adsorbent for separating U(VI) from multicomponent system. For

interfering cations ($C = 50 \text{ mg/L}$), the response of Hap@BC to high valence cations (Al^{3+} and Ca^{2+}) was stronger than monovalent cations (K^+ and Na^+), which could be attributed to the fact that high valence cations were relatively easy to be bound caused by the excess number of electrons available for interaction comparing with monovalent cations (Huang et al. 2018). On the other hand, according to the order of hydrated radius of ions, Na^+ (0.178 nm) < K^+ (0.201 nm) < Mg^{2+} (0.300 nm) < Zn^{2+} (0.404 nm) < Ca^{2+} (0.412 nm) < Al^{3+} (0.480 nm) (Tansel et al. 2006; Tansel 2012), Al^{3+} ions were preferentially bound by Hap@BC due to the bigger hydrated radius. In the adsorption process, the large hydrated radius of the adsorbate compressed the double electron layer of adsorbent, resulting in the aggregation of adsorbent, which would decrease the availability of the active site (Hui et al. 2005; Zhou et al. 2021). For co-existing anions ($C = 50 \text{ mg/L}$), the separation of U(VI) on Hap@BC was evidently inhibited by CO_3^{2-} and PO_4^{3-} , which was attributed to the formation of the soluble U(VI) species caused by the strong complexation between $\text{CO}_3^{2-}/\text{PO}_4^{3-}$ and U(VI), such as UO_2CO_3 , $\text{UO}_2(\text{CO}_3)_2^{2-}$, UO_2PO_4^- and UO_2HPO_4 (Fig. 3c and d). In summary, the process of U(VI) removal on Hap@BC was unaffected by most of interfering ions and Hap@BC could effectively and selectively adsorb U(VI) from water, which meant that Hap@BC possessed good application potential in separating U(VI) from wastewater.

Generally, the concentration of interfering ions in actual wastewater was high (Yin et al. 2019; Huang et al. 2020). In this study, the removal behavior of Hap@BC to U(VI) under different ionic strength (5, 50, 500 mg/L) was studied. For NaNO_3 (Fig. 3e), even if the concentration of NaNO_3 increased to 500 mg/L, the removal efficiency of Hap@BC remained constant, indicating that the adsorption of U(VI) on Hap@BC was mainly controlled by inner-sphere surface complexation process and the chemical bonds were formed between U(VI) and active functional groups on Hap@BC (Han et al. 2018). For $\text{Ca}(\text{NO}_3)_2$ and $\text{Al}(\text{NO}_3)_3$ (Fig. 3f and Figure S4), as the concentration of Al^{3+} and Ca^{2+} increased, the adsorption percentage for U(VI) on Hap@BC significantly decreased. Comparing with Ca^{2+} , Al^{3+} had obvious inhibition on the removal ability of Hap@BC, which further indicated that the adsorbent preferentially adsorbed the ions with large hydration radius. It was worth mentioning that Hap@BC-10% still had a certain removal efficiency for U(VI) at high ionic strength, which revealed that there were enough active sites on Hap@BC-10% for its application potential in separating U(VI).

3.2.3 Effect of contact time and initial concentration

The influence of contact time on U(VI) adsorption by Hap@BC-5%, Hap@BC-10% and Hap@BC-15% is displayed in Fig. 4a. Hap@BC-5%, Hap@BC-10% and Hap@

BC-15% responded strongly to U(VI) within the first 2 min and reached adsorption equilibrium within 5 min. It was encouraging that Hap@BC-10% displayed a favorable adsorption process and the removal percentage was close to 100% (98.7%), indicating that Hap@BC-10% possessed excellent removal ability for U(VI). The high efficiency of Hap@BC-10% for U(VI) removal was probably traceable in the abundant surface functional groups, which could offer sufficient binding sites for U(VI).

The relationship between equilibrium concentration of adsorbate in solution and adsorption capacity was very central for understanding the removal behavior and optimizing the removal process (Song et al. 2019; Zhang et al. 2018). Figure 4b shows the effect of initial U(VI) concentration on the adsorption behavior of Hap@BC. The loading of U(VI) on the adsorbent increased significantly with the increase of initial concentration. At relatively high U(VI) concentration, the adsorption capacity reached equilibrium, indicating that the available binding sites on Hap@BC-5%, Hap@BC-10% and Hap@BC-15% reached saturation (Sureshkumar et al. 2010). Comparing with Hap@BC-5% and Hap@BC-15%, the experimental value of Q_m of Hap@BC-10% was 772.8 mg/g, exceeding that of Hap@BC-5% (567.6 mg/g) and Hap@BC-15% (667.6 mg/g). This might be because Hap was evenly loaded on biocarbon in Hap@BC-10% and Hap did not agglomerate due to the appropriate addition amount, while the agglomeration of Hap particles occurred in Hap@BC-15%. For Hap@BC-5%, its effective active sites were relatively less, which resulted in a lower adsorption capacity than Hap@BC-10%. In a word, Hap@BC-10% was a more efficient adsorbent for U(VI) due to its relatively high adsorption capacity.

3.2.4 Effect of adsorbent dosage

The dosage of Hap@BC-5%, Hap@BC-10% and Hap@BC-15% would lead to the change of removal percentage (Zhang et al. 2017). As shown in Figure S5, the adsorption percentage of U(VI) on Hap@BC-5%, Hap@BC-10% and Hap@BC-15% increased to 99% when the dosage increased to a certain amount, which might be partly explained by the fact that the high dosage of Hap@BC-5%, Hap@BC-10% and Hap@BC-15% supplied enough effective active sites. It was worth mentioning that the adsorption efficiency for U(VI) on Hap@BC-10% exceeded 99.8% and the concentration of residual U(VI) in solution was less than 10 $\mu\text{g/L}$ ($C_i = 5 \text{ mg/L}$, $\text{pH} = 3$ and $m/V > 0.3 \text{ g/L}$), reaching the limit value of the World Health Organization (30 $\mu\text{g/L}$). The result revealed that Hap@BC-10% possessed great prospects in removing U(VI) from wastewater.

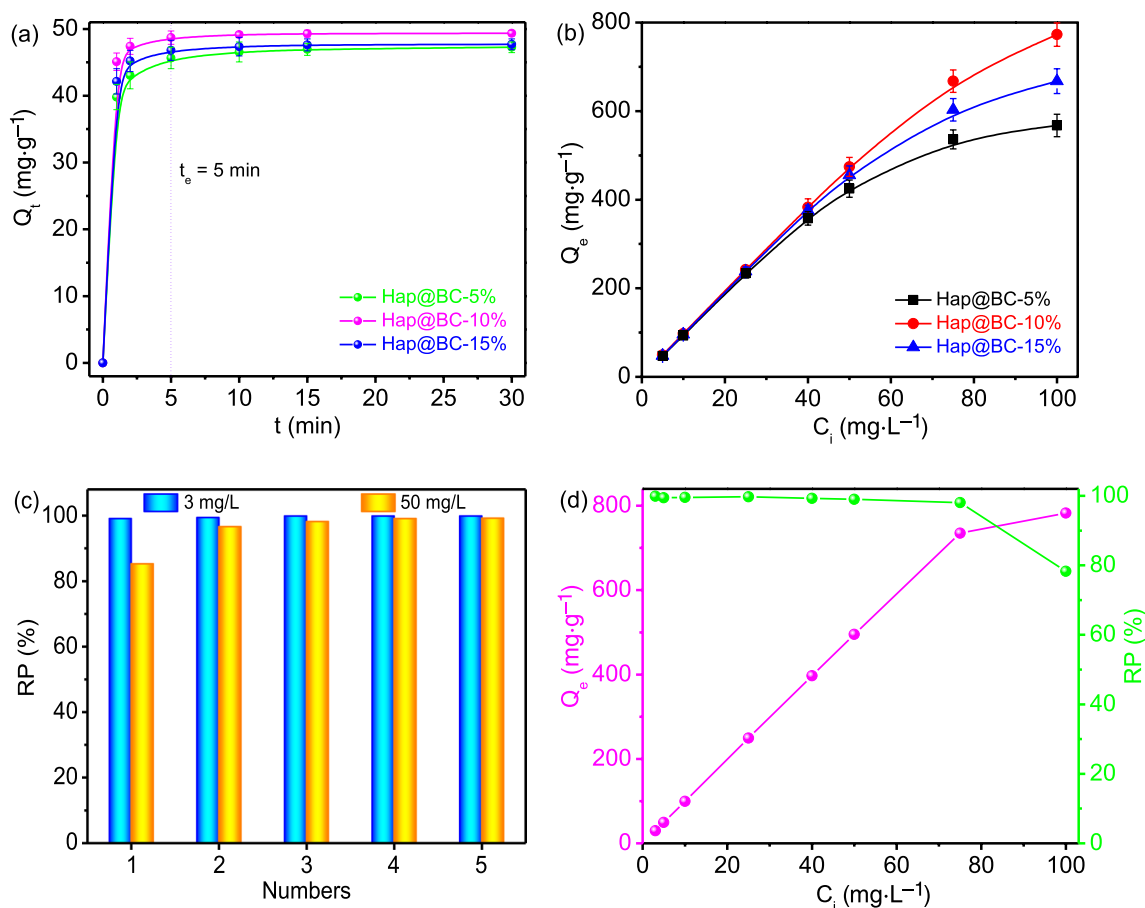


Fig. 4 **a** Effect of contact time on static U(VI) removal by Hap@BC-5%, Hap@BC-10% and Hap@BC-15% ($T=298\text{ K}$, $\text{pH}=3$, $m/V=0.1\text{ g/L}$ and $C_i=5\text{ mg/L}$), **b** Effect of initial U(VI) concentration on static U(VI) removal by Hap@BC-5%, Hap@BC-10% and Hap@BC-15% ($T=298\text{ K}$, $\text{pH}=3$ and $m/V=0.1\text{ g/L}$), **c** Removal

percentage of U(VI) on Hap@BC-10% for five times dynamic adsorption processes ($T=298\text{ K}$, $\text{pH}=3$ and $m/V=0.1\text{ g/L}$) and **d** Effect of initial U(VI) concentration on dynamic U(VI) removal by Hap@BC-10% ($T=298\text{ K}$, $\text{pH}=3$ and $m/V=0.1\text{ g/L}$)

3.2.5 Dynamic adsorption

The U(VI) removal capacity and efficiency of Hap@BC-10% were higher than those of Hap@BC-5% and Hap@BC-15%. Therefore, a self-made filter (Figure S6) was applied to further research the dynamic removal behavior of Hap@BC-10% for U(VI). In dynamic adsorption process, the flow rate of the liquid remained constant and it was not affected by the external conditions. 1.0 L U(VI)-containing liquid repeatedly flowed through the filter with 100 mg Hap@BC-10% for 5 times to complete the dynamic adsorption process. As shown in Fig. 4c, the U(VI) was completely removed in the solution with $C_i=3\text{ mg/L}$ after the solution was circulated once. For the U(VI) solution with $C_i=50\text{ mg/L}$, the adsorption efficiency was 90.4% after the solution was circulated once and the adsorption efficiency increased to 99.1% with the increase of cycle times (4 times). Figure 4d shows the relationship between adsorption capacity/efficiency and initial U(VI) concentration. The separation

efficiencies of Hap@BC-10% for U(VI) were above 99.0% at low concentrations ($C_i < 50\text{ mg/L}$). In other words, Hap@BC-10% could nearly completely separate U(VI) from water at low concentrations, further proving that Hap@BC-10% was a potential material to separate U(VI) for large-scale application. As the initial U(VI) concentration rose to 75 and 100 mg/L, the removal capacity of Hap@BC-10% for U(VI) achieved 735.2 and 782.8 mg/g and the removal efficiency was only 98.0% and 78.3%, which might be attributed to the fact that the active sites on Hap@BC-10% were almost completely occupied by U(VI). Therefore, it could be considered that Hap@BC-10% would be an ideal adsorbent for separating U(VI) owing to its high dynamic removal capacity and efficiency.

3.2.6 Adsorption kinetics and isotherms

For analyzing the control steps of adsorption process, intra-particle diffusion, Elovich, pseudo-second-order (PSO)

and pseudo-first-order (PFO) kinetic models were used to match the experimental data (Equations S1 ~ S6) (Zhang et al. 2020; Yuan et al. 2020). The PFO can well describe the physical adsorption behavior, the PSO presumes that the rate-limiting step is essentially chemisorption, the Elovich kinetic model considers that the rate-controlling step is the diffusion of the target ions and the intraparticle diffusion kinetic model assumes that the internal diffusion is a velocity-controlled step (Liao et al. 2020). As shown in Fig. 5, Figure S7 and Table 1, the Q_e of PSO was close to the experimental value and the correlation coefficient (R^2) was relatively high comparing with PFO and PSO model also displayed that the adsorption rate was proportional to the square of unoccupied active sites. In other words, PSO model could be relatively well to describe the removal for U(VI) by Hap@BC, clarifying that chemical adsorption dominated the U(VI) removal process (Zhao et al. 2019; Abdelwahab et al. 2015). As shown in Fig. 5c, the adsorption process of U(VI) on Hap@BC contained two stages.

Table 1 Kinetic parameters of U(VI) adsorption on Hap@BC-5%, Hap@BC-10% and Hap@BC-15%

Models	Parameters	Samples		
		Hap@BC-5%	Hap@BC-10%	Hap@BC-15%
PFO	K_1 (min^{-1})	1.879	2.511	2.195
	Q_e ($\text{mg}\cdot\text{g}^{-1}$)	46.2	48.9	47.1
	R^2	0.995	0.998	0.998
PSO	K_2 ($\text{g}\cdot\text{min}^{-1}\cdot\text{mg}^{-1}$)	0.107	0.204	0.153
	Q_e ($\text{mg}\cdot\text{g}^{-1}$)	47.5	49.6	48.0
	R^2	0.999	0.999	0.999
Elovich	α	4.03×10^8	7.48×10^{16}	2.80×10^{12}
	β	0.464	0.840	0.650
	R^2	0.997	0.998	0.997

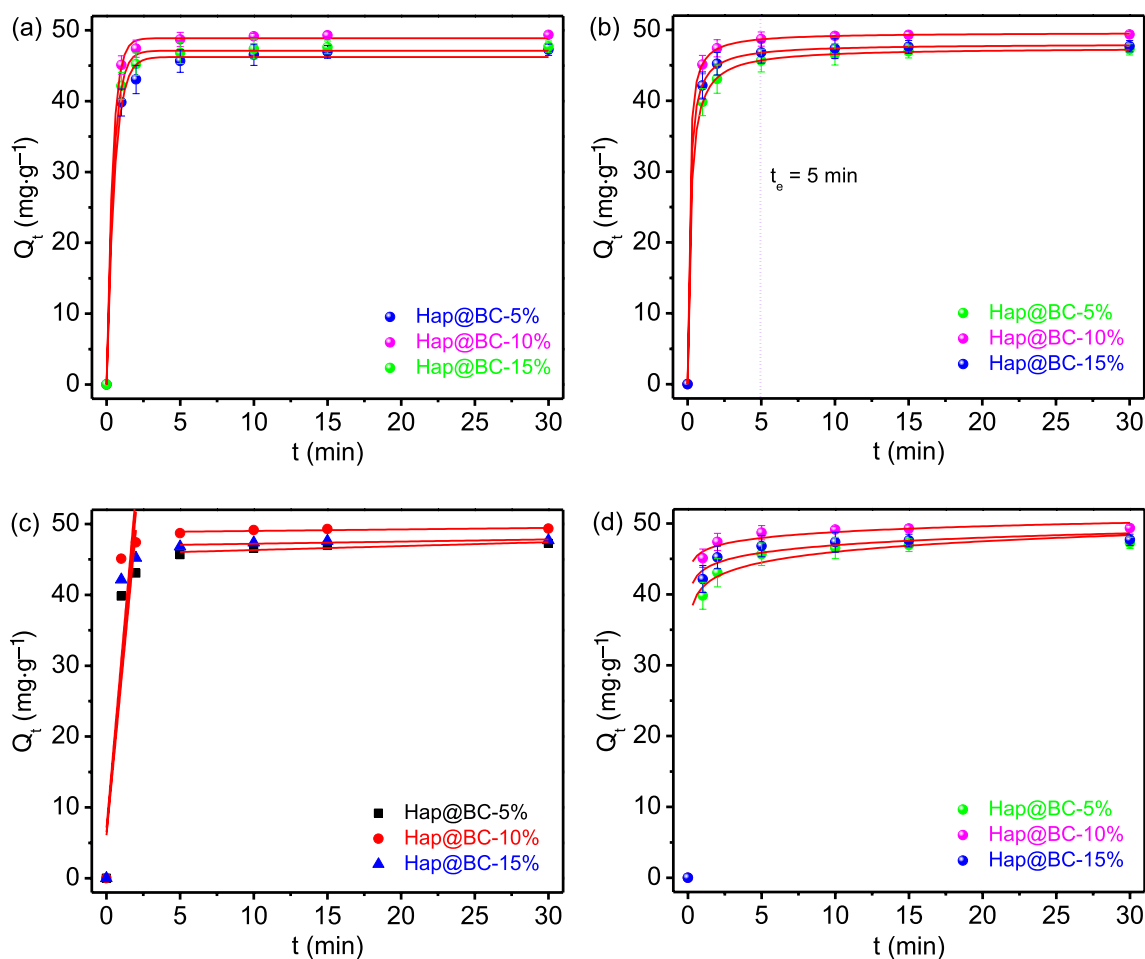


Fig. 5 Adsorption kinetic models: **a** Nonlinear PFO model, **b** Nonlinear PSO model, **c** Intraparticle diffusion model and **d** Elovich model ($C_i = 5 \text{ mg/L}$, $\text{pH} = 3$, $m/V = 0.1 \text{ g/L}$ and $T = 298 \text{ K}$)

The first stage was the dispersion of U(VI) species to the surface of Hap@BC and the second stage occurred inside of them (Yang et al. 2021). It was noteworthy that the curves did not pass through the origin, showing that the intraparticle diffusion was not the only speed-control factor (Ren et al. 2016). For Elovich kinetic model (Fig. 5d), the value of β was much smaller than α , showing that the equilibrium time of the adsorption process was relatively short. All in all, the speeding-control factor of adsorption process include chemical bonding and intraparticle diffusion.

The isotherm models were used to study the removal behavior for U(VI) (Equations S7~S12) (Kushwaha et al. 2020; Zhang et al. 2021), including Langmuir, Freundlich, Sips and Redlich–Peterson (R–P) isotherm models. The Langmuir model assumes that monolayer adsorption takes place on the homogenous surfaces, and the Freundlich isotherm is applied to represent the multilayer adsorption on heterogamous surfaces. The Sips and R–P models are hybrid model combining the Langmuir and Freundlich models and they are the most applicable 3-parameter isotherm models for monolayer adsorption (Liao and Zhang 2020). The related parameters are listed in Table 2 and the fitted curves are displayed in Fig. 6. The results illustrated that the correlation coefficient (R^2) of the Langmuir model approached to 1, which was higher than the other models, showing that the Langmuir model was suitable for fitting the removal behavior of Hap@BC to U(VI). Besides, the experimental value of Q_e was near to the fitting value from Langmuir. These results revealed that the U(VI) removal process by Hap@BC was controlled by a homogeneous

monolayer adsorption. Moreover, the adsorption capacity of Hap@BC-5%, Hap@BC-10% and Hap@BC-15% reached 606.6, 834.8, 711.9 mg/g, respectively, which were much higher comparing with other materials (Table S1).

3.2.7 Desorption and regeneration of Hap@BC-10%

The reusability of Hap@BC-10% was important to reduce the use-cost in application. For exploring the regeneration of Hap@BC-10%, different CaCl_2 solutions were used as the desorption reagents. As shown in Fig. 7a and b, the pH and concentration of the CaCl_2 solution were the important factors affecting the desorption process. With the increase of CaCl_2 concentration, the desorption efficiency for U(VI) in solution became higher, which might reveal that ion exchange was the main interaction mechanism in the adsorption process. In other words, the chemical reaction proceeded towards the direction of generating adsorbent in the desorption process due to the large amount of Ca^{2+} in the solution. In addition, U(VI) species were relatively easy to be released in acidic solution, which was attributed to the intense competition of Ca^{2+} for the binding sites in the solution with high Ca^{2+} concentration, resulting in high desorption efficiency for U(VI) in acidic CaCl_2 solution. About 99.1% of the captured U(VI) was leached in the CaCl_2 solution with the concentration of 0.1 mol/L and $\text{pH} = 1$, which would be beneficial to the recovery of U(VI). The adsorption and desorption efficiency of Hap@BC-10% for U(VI) removal remained above 93.2% and 94.6%, respectively, even after five regeneration processes (Fig. 7c and d), which

Table 2 Fitting parameters for isotherm adsorption models

Models	Adsorbents	Parameters			
		Q_m ($\text{mg}\cdot\text{g}^{-1}$)	K_L ($\text{L}\cdot\text{g}^{-1}$)	–	R^2
Langmuir	Hap@BC-5%	606.6	0.337	–	0.996
	Hap@BC-10%	834.8	0.505	–	0.998
	Hap@BC-15%	711.9	0.410	–	0.998
		–	K_F ($(\text{mg}\cdot\text{g}^{-1})(\text{L}\cdot\text{mg}^{-1})^n$)	n_F	R^2
Freundlich	Hap@BC-5%	–	189.9	3.149	0.885
	Hap@BC-10%	–	290.1	2.944	0.924
	Hap@BC-15%	–	229.5	3.026	0.888
		Q_m ($\text{mg}\cdot\text{g}^{-1}$)	K_S ($\text{L}\cdot\text{g}^{-1}$)	n	R^2
Sips	Hap@BC-5%	593.2	0.357	0.933	0.992
	Hap@BC-10%	1055.1	0.226	1.370	0.979
	Hap@BC-15%	665.7	0.497	0.835	0.997
		K_{RP} ($\text{L}\cdot\text{g}^{-1}$)	α	β	R^2
R–P	Hap@BC-5%	181.0	0.249	1.050	0.991
	Hap@BC-10%	972.9	2.698	0.716	0.955
	Hap@BC-15%	228.8	0.202	1.138	0.990

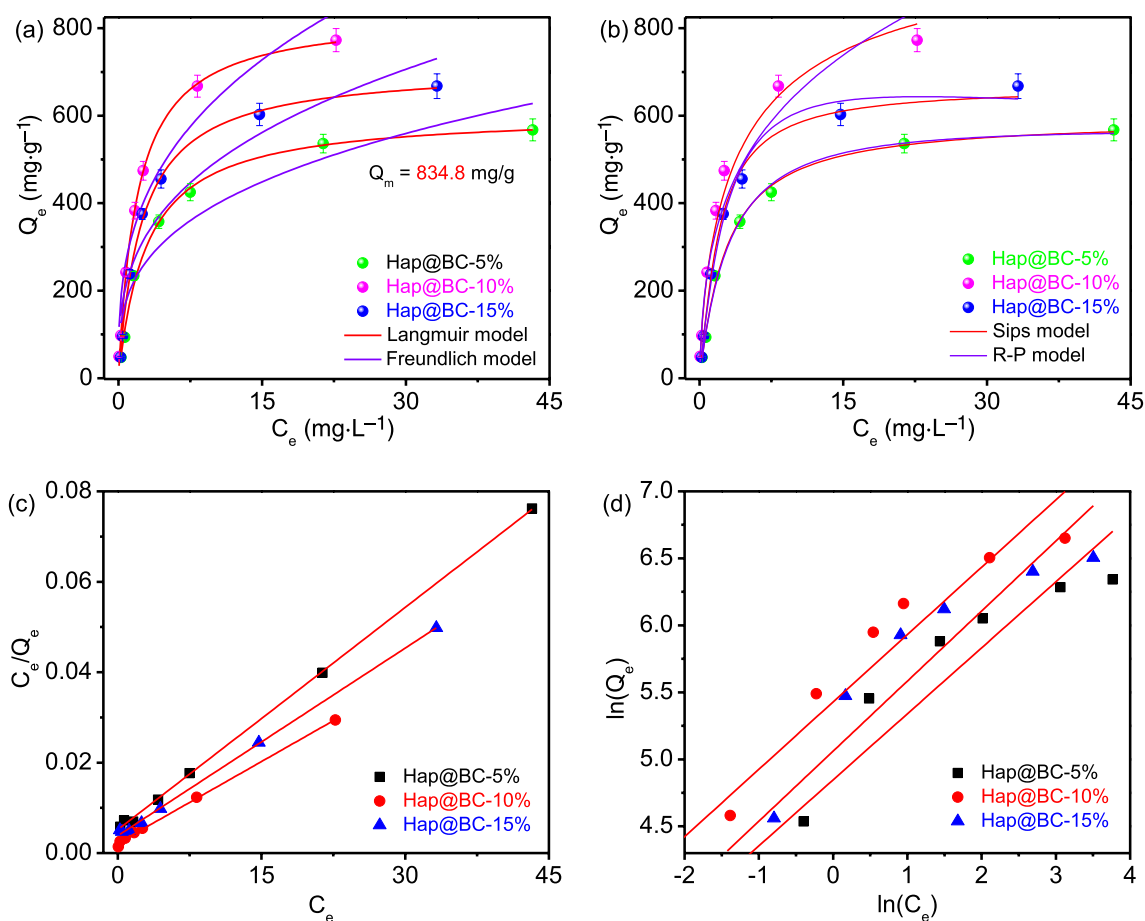


Fig. 6 Adsorption isotherm models: **a** Nonlinear Langmuir and Freundlich models, **b** Sips and R-P models, **c** Linear Langmuir model and **d** Linear Freundlich model (pH=3, m/V=0.1 g/L and T=298 K)

overcame the problem of poor reusability of Hap materials, showing that Hap@BC-10% had strong stability and excellent regeneration. In brief, Hap@BC-10% would be a truly valuable material for adsorbing U(VI) in water environment due to its excellent reusability, which has practical significance for the development and application of Hap materials.

3.3 Mechanism

3.3.1 SEM

The SEM image of Hap@BC-10% is shown in Fig. 8a. Obviously, the nHap nanoparticles (about 100 nm) with rice-like morphology were uniformly loaded on the surface of the biocarbon, providing many active adsorption sites. After adsorbing U(VI) (Fig. 8b), the rice-like morphology of nHap nanoparticles transformed into spherical morphology and the surface of the nanoparticles became rough, which was ascribed to the generation of complexes between U(VI) and the active sites on the surface of nHap nanoparticles. After desorption, the nHap nanoparticles loaded on the biocarbon

recovered to rice-like morphology and the nanoparticles were relatively smooth (Fig. 8c), which indicated that U(VI) species were resolved from the nHap nanoparticles into the solution. Moreover, the U(VI) species on Hap@BC-10%-U could be completely separated from Hap@BC-10% in the mixture of CaCl₂ (0.1 mol/L) and HCl (0.1 mol/L), which was attributed to the fact that Ca²⁺ would recapture the active sites occupied by U(VI) species and Hap@BC-10%-U would be completely restored to Hap@BC-10% in acidic solution, demonstrating that the ion exchange process was the main adsorption mechanism.

3.3.2 FT-IR and XRD

The FT-IR spectra of UO₂(NO₃)₂·6H₂O, Hap@BC-10% and Hap@BC-10%-U are shown in Fig. 8d. A new peak at 940 cm⁻¹ corresponded to the antisymmetric stretching vibration of O=U=O after U(VI) capture, indicating that U(VI) was successfully immobilized onto Hap@BC-10%. The broad peak from 480 to 700 cm⁻¹ was attributed to the bending vibrations of PO₄³⁻ (Beh et al. 2021; Kong et al.

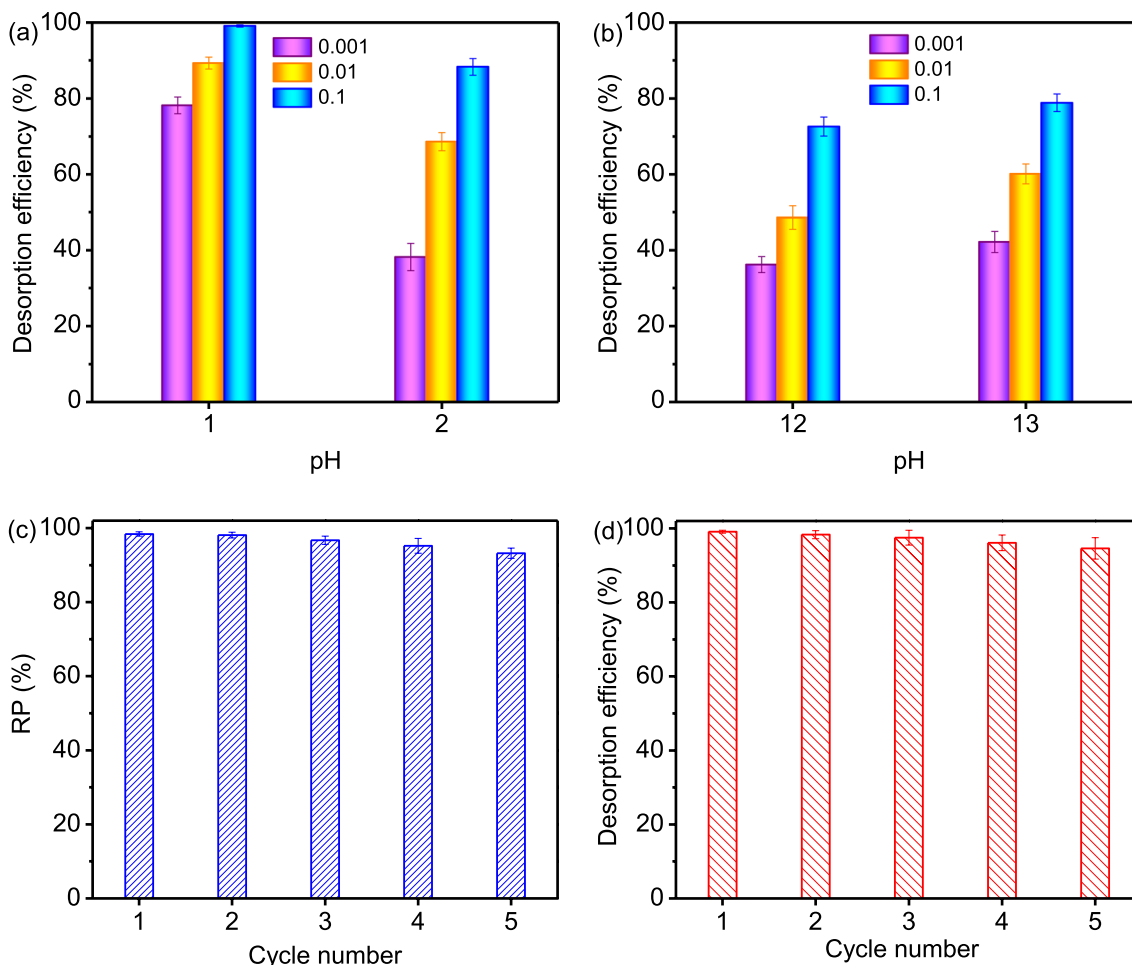


Fig. 7 **a** Effect of CaCl₂ concentration in acidic solution on desorption efficiency of Hap@BC-10%-U, **b** Effect of CaCl₂ concentration in alkaline solution on desorption efficiency of Hap@BC-10%-U,

c Removal percentage of U(VI) on Hap@BC-10% for five cycles (C_i=5 mg/L, pH=3, m/V=0.1 g/L and T=298 K) and **d** Desorption efficiency of U(VI) on Hap@BC-10%-U for five cycles

2020), which shifted to low wavenumber after adsorption, indicating that PO₄³⁻ played an important role in the adsorption for U(VI) (Guo et al. 2020b). The XRD patterns of Hap@BC-10% and Hap@BC-10%-U are shown in Fig. 8e. After adsorption, the weak peaks at 8.8° and 10.8° were observed, which were attributed to the immobilization of U(VI) by the adsorption sites on Hap@BC-10%, showing that new substances were formed on the surface of Hap@BC-10% after adsorption (Ma et al. 2019).

3.3.3 XPS

The XPS spectra of Hap@BC-10% and Hap@BC-10%-U are shown in Fig. 9a to quest the removal mechanism. After U(VI) capture, a new peak emerged at near 390 eV, which was attributed to the capture of U(VI) through chemical bonding, confirming that U(VI) was successfully immobilized on Hap@BC-10%. Besides, the high-resolution of U4f could be fitted in the form of U⁶⁺ with

binding energies of 393.0 eV (U4f_{5/2}) and 382.2 eV (U4f_{7/2}) (E_b> 382.0 eV) (Fig. 9b), proving no presence of redox reaction from U(VI) to U(IV) in the process of uranium adsorption (Guo et al. 2020b). The O1s could be separated into three peaks, corresponding to the C=O/P=O at 532.4 eV, the -OH at 530.9 eV and the bound water at 530.3 eV, respectively (Liao et al. 2022a). After U(VI) removal, the position and relative ratio of the binding energy of these O donors changed and the binding energies of -OH and C=O/P=O were moved to relatively high values owing to the decrease of electron cloud density surrounding O atoms (Fig. 9c), illustrating that the oxygen-containing groups were the essential active sites for removing U(VI) (Liu et al. 2021; Zheng et al. 2020). The binding energy of P2p shifted from 132.8 to 133.1 eV (Fig. 9d), indicating that Ca in Hap particles might be replaced in-situ by UO₂²⁺ to form the P-U bonds, which resulted in the increase of the extranuclear electron cloud density around P atoms (Ma et al. 2021). This conclusion was confirmed by the shift of the binding energy

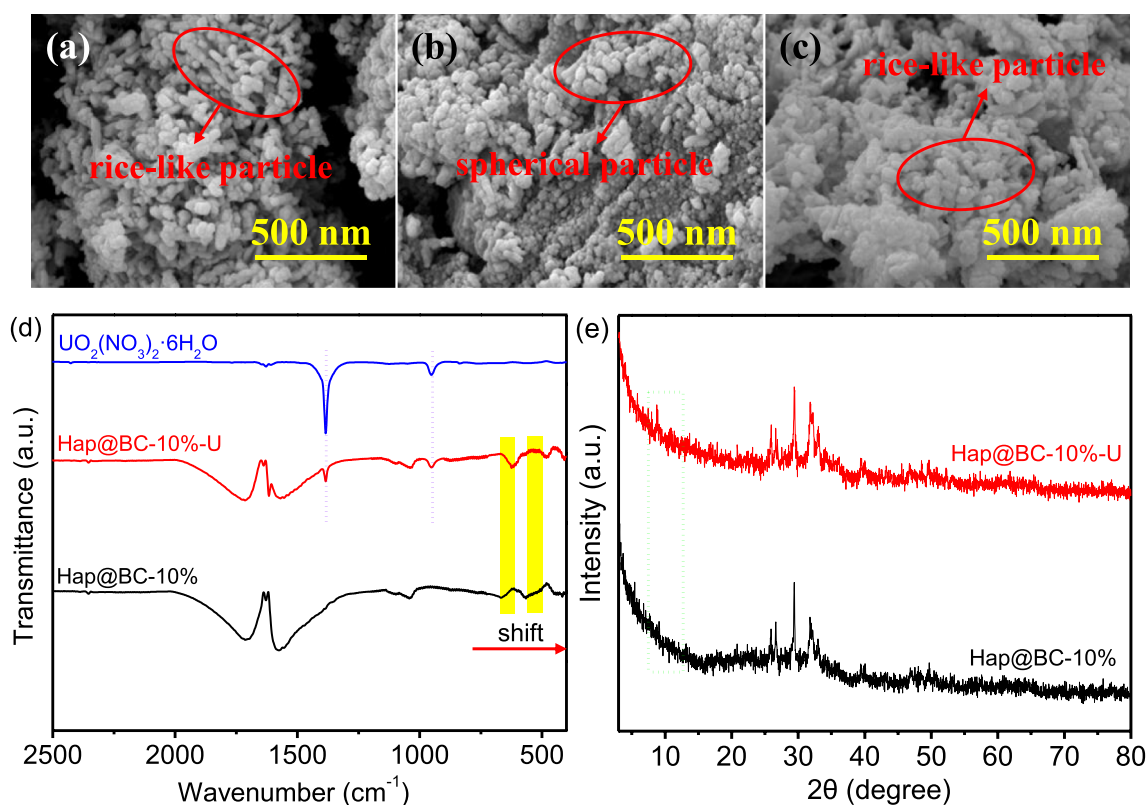
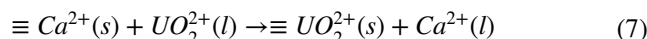
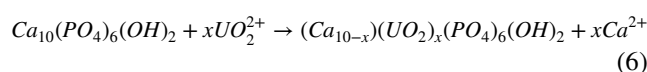
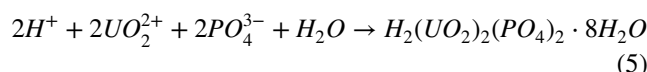
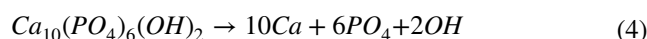
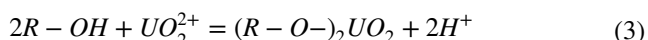


Fig. 8 **a** SEM image of Hap@BC-10%, **b** SEM image of Hap@BC-10%-U, **c** SEM image of Hap@BC-10%-U after desorption, **d** FT-IR spectra of Hap@BC-10%, Hap@BC-10%-U and $UO_2(NO_3)_2 \cdot 6H_2O$ and **e** XRD patterns of Hap@BC-10% and Hap@BC-10%-U

of Ca2p. The intensity of binding energy of Ca2p reduced by about 7% after adsorption and the binding energies of Ca2p_{1/2} and Ca2p_{3/2} increased from 346.9 and 350.5 eV to 347.1 and 350.7 eV, respectively (Fig. 9e) (Xiong et al. 2022), which further proved that Ca²⁺ in Hap was substituted in-situ by U(VI), revealing that the ion exchange occupied a crucial position in the adsorption of U(VI) on Hap@BC-10%.

In summary, Hap@BC-10% possessed an excellent adsorption property for U(VI) in solution, which could be attributed to the following reasons: (1) The surface of Hap@BC-10% was rich in acidic functional groups. (2) The strong response between Hap nanoparticles and U(VI) species. (3) Hap@BC-10% possessed the characteristics of fluffy, porous and high specific surface area, as displayed in Fig. 9f. At pH=3, due to the various active sites, U(VI) species could be immobilized on Hap@BC-10% in many ways, including electrostatic attraction, complexation (Eq. 3), ionization-precipitation (Eqs. 4 and 5) and ion exchange (Eqs. 6 and 7) (Liao et al. 2022b; Liang et al. 2017).



4 Conclusion

In conclusion, Hap@BC was successfully obtained via a simple pyrolysis technology for efficiently removing U(VI). Hap@BC showed noticeable advantages in adsorption, including good selectivity, fast adsorption rate, high removal percentage and high adsorption capacity for U(VI). The static state adsorption behavior of Hap@BC-10% to U(VI) reached the equilibrium within 5 min with the removal percentage of 98.7% ($C_i = 5$ mg/L, pH=3, m/V=0.1 g/L and T=298 K) and the maximum adsorption capacity of 834.8 mg/g (pH=3, m/V=0.1 g/L and T=298 K), which

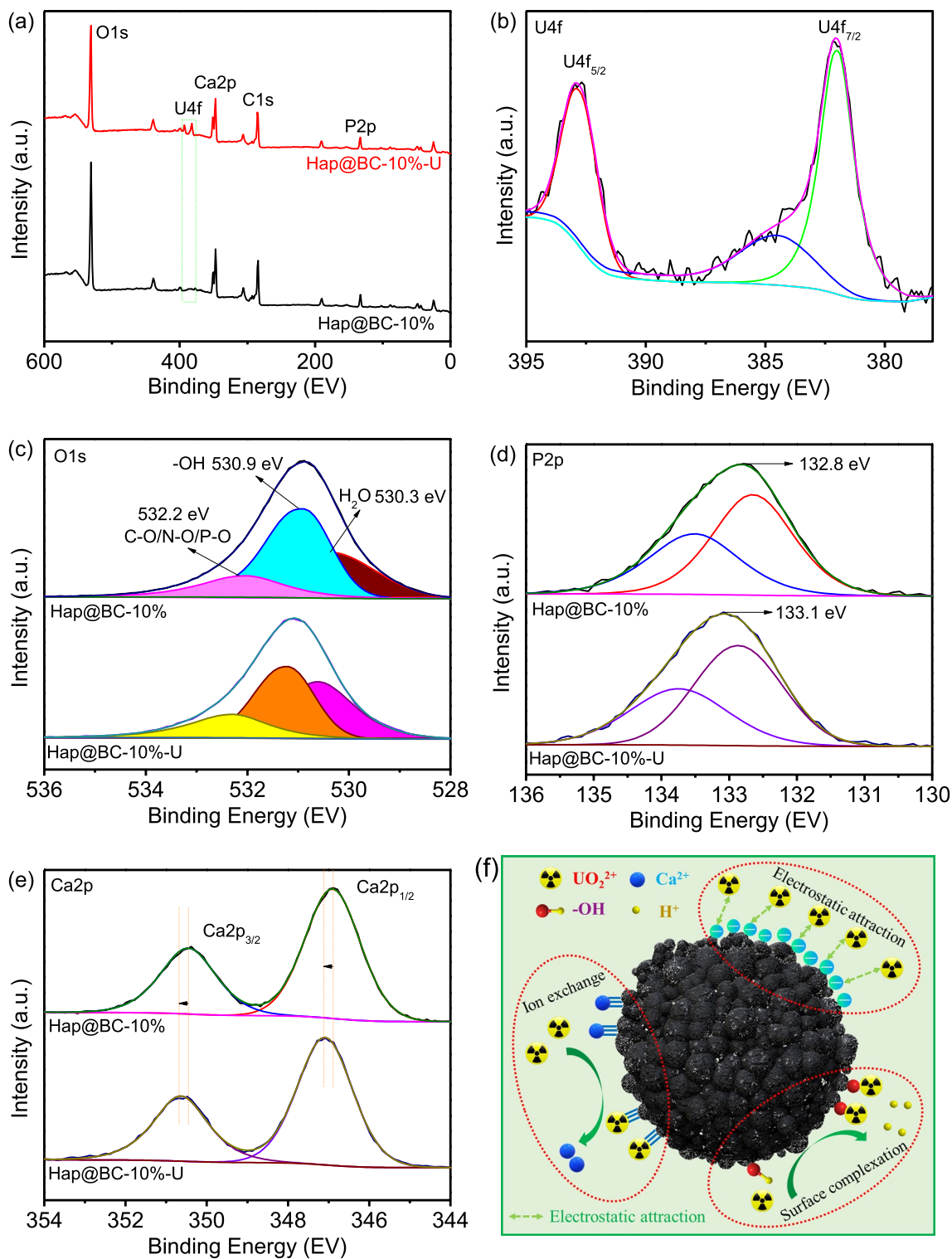


Fig. 9 **a** XPS spectra of Hap@BC-10% and Hap@BC-10%-U, **b** High-resolution XPS spectra of U4f, **c** High-resolution XPS spectra of O1s, **d** High-resolution XPS spectra of P2p, **e** High-resolution XPS spectra of Ca2p and **f** Adsorption mechanism

were similar to the results of dynamic adsorption experiments. These experimental results far exceeded other reported Hap materials. Besides, Hap@BC-10% possessed

excellent recyclability. After 5 times of adsorption–desorption processes with the mixture of HCl (0.1 mol/L) and CaCl₂ (0.1 mol/L), the adsorption efficiency was still over

93.2% ($C_i = 5 \text{ mg/L}$, $\text{pH} = 3$, $\text{m/V} = 0.1 \text{ g/L}$ and $T = 298 \text{ K}$), which provided a new design idea for the regeneration of Hap materials. In a word, this study provided an effective strategy for the development of Hap-biocran composites with high efficiency and recyclability for separating U(VI) from wastewater.

Supplementary Information The online version contains supplementary material available at <https://doi.org/10.1007/s42773-022-00154-1>.

Acknowledgements We are grateful to China Academy of Engineering Physics.

Author contributions JL: Methodology, investigation, writing-original draft; TX: Methodology, data curation, investigation; LD, YX and WZ: Data curation, investigation; YZ: Resources, writing-reviewing and editing, supervision. All authors read and approved the final manuscript.

Funding This work was financially supported by the National Natural Science Foundation of China (No. 21902130 and 21976147), Sichuan Science and Technology Program (No. 2020JDJQ0009, 2020ZDZX0012, 2020JDRC0099, 2020YFG0467 and 2020YFS0345), the Career Development Funding of CAEP (2402001), the Presidential Funding of CAEP (YZJLX2019007), Research Fund of SWUST for Ph.D. (No. 19zx7129, 18zx7149 and 17zx7135), Sichuan's Training Program of Innovation and Entrepreneurship for Undergraduate (No. S202110619086 and S202110619061).

Data availability All data generated or analysed during this study are included in this published article.

Declarations

Competing interests The authors declare that they have no known competing financial interests or personal relationships that could have appeared to influence the work reported in this paper.

Open Access This article is licensed under a Creative Commons Attribution 4.0 International License, which permits use, sharing, adaptation, distribution and reproduction in any medium or format, as long as you give appropriate credit to the original author(s) and the source, provide a link to the Creative Commons licence, and indicate if changes were made. The images or other third party material in this article are included in the article's Creative Commons licence, unless indicated otherwise in a credit line to the material. If material is not included in the article's Creative Commons licence and your intended use is not permitted by statutory regulation or exceeds the permitted use, you will need to obtain permission directly from the copyright holder. To view a copy of this licence, visit <http://creativecommons.org/licenses/by/4.0/>.

References

- Abdelwahab NA, Ammar NS, Ibrahim HS (2015) Graft copolymerization of cellulose acetate for removal and recovery of lead ions from wastewater. *Int J Biol Macromol* 79:913–922
- Ahmad M, Chen J, Yang K, Shah T, Naik M, Zhang Q, Zhang B (2021) Preparation of amidoxime modified porous organic polymer flowers for selective uranium recovery from seawater. *Chem Eng J* 418:129370
- Ahmed W, Núñez-Delgado A, Mehmood S, Ali S, Qaswar M, Shakoor A, Chen DY (2021) Highly efficient uranium (VI) capture from aqueous solution by means of a hydroxyapatite-biochar nanocomposite: adsorption behavior and mechanism. *Environ Res* 201:111518
- Beh CY, Cheng EM, Mohd Nasir NF, Khor SF, Eng SK, Abdul Majid MS, Ridzuan MJM, Lee KY (2021) Low frequency dielectric and optical behavior on physicochemical properties of hydroxyapatite/cornstarch composite. *J Colloid Interface Sci* 600:187–198
- Biedrzycka A, Skwarek E, Hanna UM (2021) Hydroxyapatite with magnetic core: synthesis methods, properties, adsorption and medical applications. *Adv Coll Interface Sci* 291:102401
- Chen C, Zhang X, Jiang T, Li M, Peng Y, Liu X, Ye J, Hua Y (2021a) Removal of uranium(VI) from aqueous solution by Mg(OH)₂-coated nanoscale zero-valent iron: reactivity and mechanism. *J Environ Chem Eng* 9:104706
- Chen Y, Li M, Li Y, Liu Y, Chen Y, Li H, Li L, Xu F, Jiang H, Chen L (2021b) Hydroxyapatite modified sludge-based biochar for the adsorption of Cu²⁺ and Cd²⁺: adsorption behavior and mechanisms. *Bioresour Technol* 321:124413
- Choong CE, Wong KT, Jang SB, Saravanan P, Park C, Kim SH, Jeon BH, Choi J, Yoon Y, Jang M (2021) Granular Mg-Fe layered double hydroxide prepared using dual polymers: insights into synergistic removal of As(III) and As(V). *J Hazard Mater* 403:123883
- Dong L, Li S, Jin Y, Hu B, Sheng G (2021) Enhanced adsorption of Eu(III) from wastewater using Solidago canadensis-derived biochar functionalized by Ca/Al-LDH and hydroxyapatite. *Appl Surf Sci* 567:150794
- El-Maghrabi HH, Younes AA, Salem AR, Rabie K, El-shereafy E (2019) Magnetically modified hydroxyapatite nanoparticles for the removal of uranium (VI): preparation, characterization and adsorption optimization. *J Hazard Mater* 378:120703
- Ferreira CRD, Santiago AAG, Vasconcelos RC, Paiva DDF, Pirih FQ, Araújo AA, Motta FV, Bomio MRD (2022) Study of microstructural, mechanical, and biomedical properties of zirconia/hydroxyapatite ceramic composites. *Ceram Int* 48:12376–12386
- Guo X, Yang H, Liu Q, Liu J, Chen R, Zhang H, Yu J, Zhang M, Li R, Wang J (2020a) A chitosan-graphene oxide/ZIF foam with anti-biofouling ability for uranium recovery from seawater. *Chem Eng J* 382:122850
- Guo Y, Gong Z, Li C, Gao B, Li P, Wang X, Zhang B, Li X (2020b) Efficient removal of uranium (VI) by 3D hierarchical Mg/Fe-LDH supported nanoscale hydroxyapatite: a synthetic experimental and mechanism studies. *Chem Eng J* 392:123682
- Han B, Zhang E, Cheng G, Zhang L, Wang D, Wang X (2018) Hydrothermal carbon superstructures enriched with carboxyl groups for highly efficient uranium removal. *Chem Eng J* 338:734–744
- Han K, Sathiyaseelan A, Saravanakumar K, Wang M (2022) Wound healing efficacy of biocompatible hydroxyapatite from bovine bone waste for bone tissue engineering application. *J Environ Chem Eng* 10:106888
- Hassanein TF, Masoud AM, Mohamed WS, Taha MH, Guibal E (2021) Synthesis of polyamide 6/nano-hydroxyapatite hybrid (PA6/n-HAp) for the sorption of rare earth elements and uranium. *J Environ Chem Eng* 9:104731
- Hu B, Ai Y, Jin J, Hayat T, Alsaedi A, Zhuang L, Wang X (2020) Efficient elimination of organic and inorganic pollutants by biochar and biochar-based materials. *Biochar* 2:47–64
- Huang S, Pang H, Li L, Jiang S, Wen T, Zhuang L, Hu B, Wang X (2018) Unexpected ultrafast and high adsorption of U(VI) and Eu(III) from solution using porous Al₂O₃ microspheres derived from MIL-53. *Chem Eng J* 353:157–166
- Huang Q, Song S, Chen Z, Hu B, Chen J, Wang X (2019) Biochar-based materials and their applications in removal of organic

- contaminants from wastewater: state-of-the-art review. *Biochar* 1:45–73
- Huang S, Hu M, Li D, Wang L, Zhang C, Li K, He Q (2020) Fluoride sorption from aqueous solution using $\text{Al}(\text{OH})_3$ -modified hydroxyapatite nanosheet. *Fuel* 279:118486
- Hui KS, Chao CYS, Kot SC (2005) Removal of mixed heavy metal ions in wastewater by zeolite 4A and residual products from recycled coal fly ash. *J Hazard Mater* 127:89–101
- Idrees M, Batool S, Kalsoom T, Yasmeen S, Kalsoom A, Raina S, Zhuang Q, Kong J (2018) Animal manure-derived biochars produced via fast pyrolysis for the removal of divalent copper from aqueous media. *J Environ Manage* 213:109–118
- Jin T, Huang B, Huang J, He F, Liu Z, Qian Y (2021) A novel poly(amic-acid) modified single-walled carbon nanohorns adsorbent for efficient removal of uranium (VI) from aqueous solutions and DFT study. *Colloids Surf A* 631:127747
- Kede MLFM, Mavropoulos E, da Rocha NCC, Costa AM, Da-Silva MHP, Moreira JC, Rossi AM (2012) Polymeric sponges coated with hydroxyapatite for metal immobilization. *Surf Coat Technol* 206:2810–2816
- Kong L, Ruan Y, Zheng Q, Su M, Diao Z, Chen D, Hou L, Chang X, Shih K (2020) Uranium extraction using hydroxyapatite recovered from phosphorus containing wastewater. *J Hazard Mater* 382:120784
- Kushwaha S, Mane M, Ravindranathan S, Das A (2020) Polymer nanorings with uranium specific clefts for selective recovery of uranium from acidic effluents via reductive adsorption. *ACS Sens* 5:3254–3263
- Lei J, Liu H, Yuan C, Chen Q, Liu J, Wen F, Jiang X, Deng W, Cui X, Duan T, Zhu W, He R (2022) Enhanced photoreduction of U(VI) on WO_3 nanosheets by oxygen defect engineering. *Chem Eng J* 416:129164
- Li Y, Li L, Chen T, Duan T, Yao W, Zheng K, Dai L, Zhu W (2018) Bioassembly of fungal hypha/graphene oxide aerogel as high performance adsorbents for U(VI) removal. *Chem Eng J* 347:407–414
- Li Z, Li M, Zheng T, Li Y, Liu X (2019) Removal of tylosin and copper from aqueous solution by biochar stabilized nano-hydroxyapatite. *Chemosphere* 235:136–142
- Li J, Tian X, Bai R, Xiao X, Yang F, Zhao F (2022) Transforming cerussite to pyromorphite by immobilising Pb(II) using hydroxyapatite and *Pseudomonas rhodesiae*. *Chemosphere* 287:132235
- Liang J, Li X, Yu Z, Zeng G, Luo Y, Jiang L, Yang Z, Qian Y, Wu H (2017) Amorphous MnO_2 modified biochar derived from aerobically composted swine manure for adsorption of Pb(II) and Cd(II). *ACS Sustain Chem Eng* 5:5049–5058
- Liang L, Xi F, Tan W, Meng X, Hu B, Wang X (2021) Review of organic and inorganic pollutants removal by biochar and biochar-based composites. *Biochar* 3:255–281
- Liao J, Zhang Y (2020) Effective removal of uranium from aqueous solution by using novel sustainable porous Al_2O_3 materials derived from different precursors of aluminum. *Inorg Chem Front* 7:765–776
- Liao J, Zhang Y, Zhang L (2020) Improved catalytic activity on the thermal decomposition of ammonium perchlorate and efficient adsorption of uranium using a novel ultra-low density Al_2O_3 -based aerogels. *J Hazard Mater* 387:122015
- Liao J, Liu P, Xie Y, Zhang Y (2021) Metal oxide aerogels: preparation and application for the uranium removal from aqueous solution. *Sci Total Environ* 768:144212
- Liao J, He X, Zhang Y, Zhu W, Zhang L, He Z (2022a) Bismuth impregnated biochar for efficient uranium removal from solution: adsorption behavior and interfacial mechanism. *Sci Total Environ* 819:153145
- Liao J, Xiong T, Ding L, Zhang Y, Zhu W (2022b) Effective separation of uranium(VI) from wastewater using a magnetic carbon as a recyclable adsorbent. *Sep Purif Technol* 282:120140
- Liu J, Shi S, Li C, Hong X, Gu Z, Li F, Zhai J, Zhang Q, Liao J, Liu N, Liu C (2021) U(VI) adsorption by one-step hydrothermally synthesized cetyltrimethylammonium bromide modified hydroxyapatite-bentonite composites from phosphate-carbonate coexisted solution. *Appl Clay Sci* 203:106027
- Liu W, Wang Q, Wang H, Xin Q, Hou W, Hu E, Lei Z (2022) Adsorption of uranium by chitosan/*Chlorella pyrenoidosa* composite adsorbent bearing phosphate ligand. *Chemosphere* 287:132193
- Londoño-Restrepo SM, Herrera-Lara M, Bernal-Alvarez LR, Rivera-Muñoz EM, Rodríguez-García ME (2020) In-situ XRD study of the crystal size transition of hydroxyapatite from swine bone. *Ceram Int* 46:24454–24461
- Ma J, Zhao Q, Zhou L, Wen T, Wang J (2019) Mutual effects of U(VI) and Eu(III) immobilization on interpenetrating 3-dimensional MnO_2 /graphene oxide composites. *Sci Total Environ* 695:133696
- Ma K, Cui H, Zhou A, Wu H, Dong X, Zu F, Yi J, Wang R, Xu Q (2021) Mesoporous hydroxyapatite: synthesis in molecular self-assembly and adsorption properties. *Microporous Mesoporous Mater* 323:111164
- Nezhad MM, Semnani A, Tavakkoli N, Shirani M (2021) Selective and highly efficient removal of uranium from radioactive effluents by activated carbon functionalized with 2-aminobenzoic acid as a new sorbent. *J Environ Manage* 299:113587
- Qin C, Deng H, Ao S, Dai Z, Huang J, Ni H, Ye P (2021) High-quality graphene derivative: hydroxylated graphene prepared by modification of aromatic ring. *Carbon* 176:290–295
- Qiu M, Hu B, Chen Z, Yang H, Zhuang L, Wang X (2021) Challenges of organic pollutant photocatalysis by biochar-based catalysts. *Biochar* 3:117–123
- Ren H, Gao Z, Wu D, Jiang J, Sun Y, Luo C (2016) Efficient Pb(II) removal using sodium alginate-carboxymethyl cellulose gel beads: preparation, characterization, and adsorption mechanism. *Carbohydr Polym* 137:402–409
- Son YR, Park SJ (2019) Effect of graphene oxide/carbon nanotube ratio on electrochemical behaviors of spongy bone-like reduced graphene oxide/carbon nanotube foam prepared by simple and green approach. *Chem Eng J* 373:1020–1029
- Song S, Wang K, Zhang Y, Wang Y, Zhang C, Wang X, Zhang R, Chen J, Wen T, Wang X (2019) Self-assembly of graphene oxide/PEDOT:PSS nanocomposite as a novel adsorbent for uranium immobilization from wastewater. *Environ Pollut* 250:196–205
- Su M, Liu Z, Wu Y, Peng H, Ou T, Huang S, Song G, Kong L, Chen N, Chen D (2021) Graphene oxide functionalized with nano hydroxyapatite for the efficient removal of U(VI) from aqueous solution. *Environ Pollut* 268:115786
- Sureshkumar MK, Das D, Mallia MB, Gupta PC (2010) Adsorption of uranium from aqueous solution using chitosan-tripolyphosphate (CTPP) beads. *J Hazard Mater* 184:65–72
- Tal OP, Mizrahi A, Lerner N, Gelfer S, Columbus I, Mizrahi D (2022) Preparation and characterization of Melamine-Formaldehyde (MF)-bound cyclen derivatives for efficient removal of uranium [U(VI)] ions from wastewater. *J Water Process Eng* 45:102448
- Tansel B (2012) Significance of thermodynamic and physical characteristics on permeation of ions during membrane separation: hydrated radius, hydration free energy and viscous effects. *Sep Purif Technol* 86:119–126
- Tansel B, Sager J, Rector T, Garland J, Strayer RF, Levine L, Roberts M, Hummerick M, Bauer J (2006) Significance of hydrated radius and hydration shells on ionic permeability during nanofiltration in dead end and cross flow modes. *Sep Purif Technol* 51:40–47

- Verma S, Kim KH (2022) Graphene-based materials for the adsorptive removal of uranium in aqueous solutions. *Environ Int* 158:106944
- Wang Y, Hu L, Zhang G, Yan T, Yan L, Wei Q, Du B (2017) Removal of Pb(II) and methylene blue from aqueous solution by magnetic hydroxyapatite-immobilized oxidized multi-walled carbon nanotubes. *J Colloid Interface Sci* 494:380–388
- Wang F, Liao Y, Xia L (2021) Poly(amidoamine) dendrimer decorated dendritic fibrous nano-silica for efficient removal of uranium (VI). *J Solid State Chem* 303:122511
- Wang Y, Peng Z, Yang Y, Li Z, Wen Y, Liu M, Li S, Su L, Zhou Z, Zhu Y, Zhou N (2022) *Auricularia auricula* biochar supported γ -FeOOH nanoarrays for electrostatic self-assembly and pH-responsive controlled release of herbicide and fertilizer. *Chem Eng J* 437:134984
- Wu Y, Chen D, Kong L, Tsang DCW, Su M (2019) Rapid and effective removal of uranium (VI) from aqueous solution by facile synthesized hierarchical hollow hydroxyapatite microspheres. *J Hazard Mater* 371:397–405
- Xiong T, Li Q, Liao J, Zhang Y, Zhu W (2022) Highly enhanced adsorption performance to uranium(VI) by facile synthesized hydroxyapatite aerogel. *J Hazard Mater* 423:127184
- Xuan K, Wang J, Gong Z, Wang X, Li J, Guo Y, Sun Z (2022) Hydroxyapatite modified ZIF-67 composite with abundant binding groups for the highly efficient and selective elimination of uranium (VI) from wastewater. *J Hazard Mater* 426:127834
- Yang Y, Zeng L, Lin Z, Jiang H, Zhang A (2021) Adsorption of Pb^{2+} , Cu^{2+} and Cd^{2+} by sulfhydryl modified chitosan beads. *Carbohydr Polym* 274:118622
- Yin L, Hu Y, Ma R, Wen T, Wang X, Hu B, Yu Z, Hayat T, Alsaedi A, Wang X (2019) Smart construction of mesoporous carbon templated hierarchical Mg-Al and Ni-Al layered double hydroxides for remarkably enhanced U(VI) management. *Chem Eng J* 359:1550–1562
- Yuan D, Zhang S, Tan J, Dai Y, Wang Y, He Y, Liu Y, Zhao X, Zhang M, Zhang Q (2020) Highly efficacious entrapment of Th (IV) and U (VI) from rare earth elements in concentrated nitric acid solution using a phosphonic acid functionalized porous organic polymer adsorbent. *Sep Purif Technol* 237:116379
- Yue Y, Liu Y, Wang J, Vukanti R, Ge Y (2021) Enrichment of potential degrading bacteria accelerates removal of tetracyclines and their epimers from cow manure biochar amended soil. *Chemosphere* 278:130358
- Zhang J, Chen S, Zhang H, Wang X (2017) Removal behaviors and mechanisms of hexavalent chromium from aqueous solution by cephalosporin residue and derived chars. *Bioresour Technol* 238:484–491
- Zhang C, Liu Y, Li X, Chen H, Wen T, Jiang Z, Ai Y, Sun Y, Hayat T, Wang X (2018) Highly uranium elimination by crab shells-derived porous graphitic carbon nitride: batch, EXAFS and theoretical calculations. *Chem Eng J* 346:406–415
- Zhang J, Zhang H, Liu Q, Song D, Li R, Liu P, Wang J (2019) Diaminomaleonitrile functionalized double-shelled hollow MIL-101 (Cr) for selective removal of uranium from simulated seawater. *Chem Eng J* 368:951–958
- Zhang S, Yuan D, Zhang Q, Wang Y, Liu Y, Zhao J, Chen B (2020) Highly efficient removal of uranium from highly acidic media achieved on a phosphine oxide and amino functionalized superparamagnetic composite polymer adsorbent. *J Mater Chem A* 8:10925–10934
- Zhang S, Yuan D, Zhao J, Ren G, Zhao X, Liu Y, Wang Y, He Y, Ma M, Zhang Q (2021) Highly efficient extraction of uranium from strong HNO_3 media achieved on phosphine oxide functionalized superparamagnetic composite polymer microspheres. *J Mater Chem A* 9:18393–18405
- Zhao B, Jiang H, Lin Z, Xu S, Xie J, Zhang A (2019) Preparation of acrylamide/acrylic acid cellulose hydrogels for the adsorption of heavy metal ions. *Carbohydr Polym* 224:115022
- Zheng N, Yin L, Su M, Liu Z, Tsang DCW, Chen D (2020) Synthesis of shape and structure-dependent hydroxyapatite nanostructures as a superior adsorbent for removal of U(VI). *Chem Eng J* 384:123262
- Zhou Y, Li W, Jiang X, Sun Y, Yang H, Liu Q, Cao Y, Zhang Y, Cheng H (2021) Synthesis of strontium (Sr) doped hydroxyapatite (HAp) nanorods for enhanced adsorption of Cr (VI) ions from wastewater. *Ceram Int* 47:16730–16736
- Zhou C, Song X, Wang Y, Wang H, Ge S (2022) The sorption and short-term immobilization of lead and cadmium by nano-hydroxyapatite/biochar in aqueous solution and soil. *Chemosphere* 286:131810
- Zhu W, Li Y, Dai L, Li J, Li X, Li W, Duan T, Lei J, Chen T (2018) Bioassembly of fungal hyphae/carbon nanotubes composite as a versatile adsorbent for water pollution control. *Chem Eng J* 339:214–222
- Zhu M, Liu L, Feng J, Dong H, Zhang C, Ma F, Wang Q (2021) Efficient uranium adsorption by amidoximized porous polyacrylonitrile with hierarchical pore structure prepared by freeze-extraction. *J Mol Liq* 328:115304